The Doping Mechanism of Halide Perovskite Unveiled by Alkaline Earth Metals

Nga Phung,[1§] Roberto Félix,[1§] Daniele Meggiolaro,[2, 3] Amran Al-Ashouri,[1] Gabrielle Sousa e Silva,[1] Claudia Hartmann,[1] Juanita Hidalgo,[4] Hans Köbler,[1] Edoardo Mosconi,[2, 3] Barry Lai,[5] Rene Gunder,[1] Meng Li,[1,6,7] Kai-Li Wang,[6] Zhao-Kui Wang,[6] Kaiqi Nie,[1, 6] Evelyn Handick,[1] Regan G. Wilks,[1] Jose A. Marquez,[1] Bernd Rech,[1, 8] Thomas Unold,[1] Juan-Pablo Correa-Baena,[4] Steve Albrecht,[1, 8] Filippo De Angelis, [2, 3, 9] Marcus Bär,[1, 10, 11] Antonio Abate[1, 12*]

1. Helmholtz-Zentrum Berlin für Materialien und Energie GmbH, Hahn-Meitner-Platz 1, 14109 Berlin, Germany.
2. Computational Laboratory for Hybrid/Organic Photovoltaics (CLHYO), CNR-ISTM, Via Elce di Sotto 8, 06123 Perugia, Italy.
3. D3-CompuNet, Istituto Italiano di Tecnologia, Via Morego 30, 16163 Genova, Italy.
4. School of Materials Science and Engineering, Georgia Institute of Technology, North Ave NW, Atlanta, Georgia 30332, USA.
5. Advanced Photon Source, Argonne National Lab, 9700 Cass Ave, Lemont, Illinois 60439, USA.
6. Institute of Functional Nano & Soft Materials (FUNSOM), Jiangsu Key Laboratory for Carbon-Based Functional Materials & Devices, Joint International Research Laboratory of Carbon-Based Functional Materials and Devices, Soochow University, Suzhou, 215123, P. R. China.
7. Laboratory of Advanced Optoelectronic Materials, College of Chemistry, Chemical Engineering and Materials Science, Soochow University, Suzhou 215123, P. R. China.
8. Faculty of Electrical Engineering and Computer Science, Technical University Berlin, Marchstraße 23, 10587 Berlin, Germany.
9. Department of Chemistry, Biology and Biotechnology, University of Perugia, Via Elce di Sotto 8, 06123, Perugia, Italy.
10. Department of Chemistry and Pharmacy, Friedrich-Alexander-Universität Erlangen-Nürnberg, Egerland Str. 3, 91058 Erlangen, Germany.
11. Helmholtz Institute Erlangen-Nürnberg for Renewable Energy (HI ERN), Albert-Einstein-Str. 15, 12489 Berlin, Germany.
12. Department of Chemical, Materials and Production Engineering, University of Naples Federico II, Piazzale Tecchio 80, 80125 Fuorigrotta, Italy.

§ NP and RF contribute equally to this work.

* Corresponding author: Antonio Abate *antonio.abate@helmholtz-berlin.de;*
antonio.abate@unina.it

Abstract

Halide perovskites are a strong candidate for the next generation of photovoltaics. Chemical doping of halide perovskites is an established strategy to prepare the highest efficiency and most stable perovskite-based solar cells. In this study, we unveil the doping mechanism of halide perovskites using a series of alkaline earth metals. We find that low doping levels enable the incorporation of the dopant within the perovskite lattice, whereas high doping concentrations induce surface segregation. The threshold from low to high doping regime correlates to the size of the doping element. We show that the low doping regime results in a more n-type material, while the high doping regime induces a less n-type doping character. Our work provides a comprehensive picture of the unique doping mechanism of halide perovskites, which differs from classical semiconductors. We proved the effectiveness of the low doping regime for the first time, demonstrating highly efficient methylammonium lead iodide based solar cells in both n-i-p and p-i-n architectures.
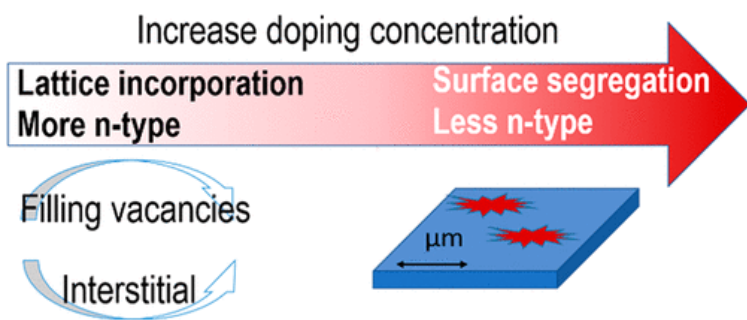
Introduction

Halide perovskite absorbers have enabled solar cells with more than 25% power conversion efficiency (PCE) on a lab-scale, which makes them potentially competitive with established thin-film technologies such as those based on CdTe and Cu(In, Ga)Se$_2$ (CIGS) absorbers.[1] This class of material has a general composition of ABX$_3$, where A is a monovalent cation (e.g. methylammonium (MA)), B is a divalent cation (e.g. Pb), and X is a halide. The so-called 3D halide perovskites consist of cation A residing in a cage made of corner sharing octahedra BX$_6$. The addition of a small number of foreign ions into the perovskite precursor solution is a well-known strategy to improve the efficiency of perovskite-based solar cells (PSCs).[2−5] In the majority of the cases, the addition of foreign ions results in the segregation at the surface of the perovskite crystals as a secondary phase, which may still have a positive impact on the device performance[6] while leaving the perovskite crystal structure unchanged.[7]

Ionic radii control whether or not foreign cations can be incorporated into the perovskite lattice. For instance, the monovalent ions Rb, K, and Na are too small to be included stably into the lattice. However, they improve PSCs performance by influencing the crystallization and the surface defect chemistry.[6,8] Divalent ions such as alkaline earth metals Sr, Ca, and Mg, or transition metals such as Cd and Co have also been explored.[2,9−13] In particular, theoretical calculations have predicted Sr^{2+} to replace Pb^{2+} in the perovskite lattice, as Sr^{2+} and Pb^{2+} have similar ionic radii, while Mg^{2+} cannot.[9,11,14,15] Sr^{2+} has enabled significant efficiency enhancement in PSCs; however, it remains unclear how much Sr^{2+} can actually be incorporated in the perovskite lattice. Considering that the ionic radii of Sr^{2+} and Mg^{2+} in bonding with six halides are 118 and 72 pm, respectively,[16] these ionic radii, thus, can be translated directly to the bond length of B-X in the octahedron of the 3D perovskite structure. In particular, Sr–I bond length is the summation of Sr^{2+} radius and I$^-$ radius. The tolerance factor is defined as $t = (r_A + r_X)/(\sqrt{2}(r_B + r_X))$,[17] where the MA$^+$ radius is taken as 217 pm and I$^-$ is 220 pm. Hence, the tolerance factor for Sr^{2+} and Mg^{2+} replacing Pb^{2+} (119 pm) in 3D MA-based perovskite structure is 0.91 and 1.06, respectively. To form a 3D perovskite structure, the tolerance factor of the compound should be in the range of 0.8 to 1.0.[18,19] Therefore, Sr^{2+} is expected to form a MASrI$_3$ 3D halide perovskite, whereas Mg^{2+} is not a suitable candidate. However, a purely synthesized 3D MASrI$_3$ halide perovskite has not yet been reported by the time of this study.[10,11] In fact, several studies have observed that Sr-doped perovskite films exhibit Sr-rich phases at the surface, which may modify the interfacial energy alignment between perovskite and the charge selective contact layers in PSCs.[20−22]

Here, we use Sr^{2+} and Mg^{2+} as representative cations to investigate the size dependence doping mechanism of halide perovskites. Combining theoretical and experimental investigations, including synchrotron-based characterizations of the materials and device integration, we identify two doping regimes. At relatively high doping levels (3–10 mol%), such as those most commonly used in literature, the dopant is likely to segregate in a secondary phase at the surface of the perovskite. Conversely, at concentrations significantly lower (0.1–1 mol%) the dopants are incorporated into the perovskite lattice. The threshold between the low- and high-doping regime depends on the size of the dopant. We show that the low doping regime induces a more n-type material while the high doping regime induces a less n-type doping character of the perovskite semiconductor. Such behavior is peculiar of halide perovskites and somewhat different from doping of classical semiconductors. We prove the low-doping regime as a new strategy to enhance the efficiency of perovskite solar cells, demonstrating MAPbI$_3$-based devices with an open circuit voltage exceeding 1.16 V and a stabilized power conversion efficiency exceeding 19% in a p-i-n and 20% in an n-i-p solar cell.

Results and Discussion

Doping Mechanism

The formation of halide perovskites is associated with the existence of lattice defects as for any crystalline material. Density functional theory (DFT) calculations have shown that Schottky defects, which form when oppositely charged ions leave their lattice sites creating vacancies, contribute to the defects density in halide perovskites most significantly.[23−25] The calculated concentration of the Schottky defects in the perovskite lattice spans from 10^{10} up to 10^{20} cm^{-3}.[23−25] Given that the Pb^{2+} concentration in a perfect perovskite crystal is in the range of 10^{21} cm^{-3}, we rationalize that the defect concentrations in halide perovskite should not be higher than 1% of the Pb^{2+}. Therefore, if chemical doping is explored for the healing of harmful defects, the doping should be in subpercent molar. However, most of the works in the literature report significantly higher doping levels to demonstrate improved PSCs performances.[13,20,21,26−28]

We hypothesize that a limited amount of dopant, which depends on the atomic size of the doping element, can be incorporated into the perovskite lattice and thus interact with the defect chemistry of the material. To demonstrate our hypothesis, we focus on Sr^{2+} and Mg^{2+} since they have similar chemical properties (elements in the same chemical group) but have different ionic radii (118 and 72 pm, respectively).[16] DFT shows that the incorporation of Sr^{2+} and Mg^{2+} in MAPbI$_3$ may occur through various processes: (i) Pb^{2+} substitution (Sr$_{Pb}$ or Mg$_{Pb}$); (ii) interstitial (Sr$_i^{2+}$ or Mg$_i^{2+}$); (iii) MA$^+$ substitution (Sr$_{MA}^+$ or Mg$_{MA}^+$) as all illustrated in Figure 1.
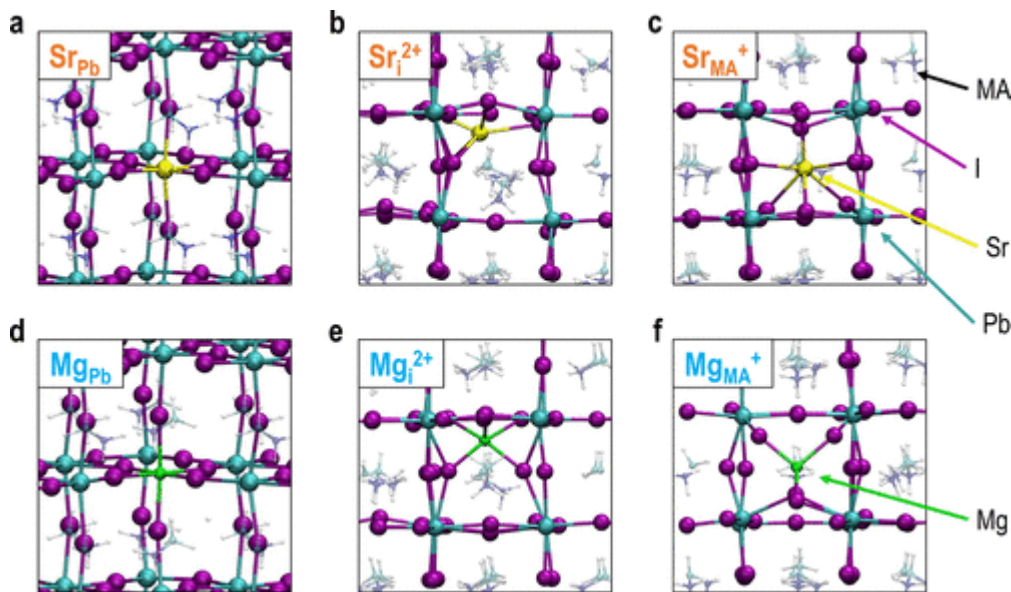
Figure 1

Figure 1. Potential doping mechanism calculated by DFT. Visualization of Sr doping (depicted in yellow) (a) Pb^{2+} substitution by Sr^{2+} (Sr$_{Pb}$), (b) interstitial Sr^{2+} (Sr$_i^{2+}$), and (c) methylammonium (MA) substitution by Sr^{2+} (Sr$_{MA}^+$). Similarly, Mg doping (depicted in green) as (d) Pb^{2+} substitution by Mg^{2+} (Mg$_{Pb}$), (e) interstitial Mg^{2+} (Mg$_i^{2+}$), and (f) MA substitution by Mg^{2+} (Mg$_{MA}^+$).

Doping in the Silicon system involves the dopants providing extra electrons or holes to the Si network.[29] Changes in intrinsic point defect concentrations that shift the Fermi level (E$_F$) occur in CIGS absorbers,[30] and to some extent are also found in halide perovskites.[31] However, this kind of doping is tuned by the growth method[32] without any extrinsic dopants like in doping of Si. Herein, to the best of our knowledge, this is the first report on doping a halide perovskite by intentional manipulation of the defect chemistry of the material by extrinsic dopants. The dopants (Sr and Mg) incorporation or segregation can change the defect concentrations in MAPbI$_3$. Depending on the doping regime, the (net) n-type doping of the perovskite is either increased or decreased. It is rather surprising that *one* dopant can introduce more or less n-type doping depending on the concentration, which is different from classical doping. The threshold between the low- and high-doping regimes depends on the size of the dopant, which will be discussed in more detail in the next sections.

Effect of Different Doping Regimes on Material Property

We employed hard X-ray photoelectron spectroscopy (HAXPES) to examine the chemical composition of doped perovskite layers. The same substrate and deposition procedure used for the preparation of PSCs were used to rule out any possible side effects (see Methods section).(33)Figure 2a,b presents the quantified [Sr]:[Pb] and [Mg]:[Pb] ratios derived from the HAXPES core levels (i.e., Sr $3p_{3/2}$, Mg 1s, and Pb $4f_{7/2}$) measured with excitation energies of 2 and 6 keV (the corresponding 2 and 6 keV excited HAXPES spectra are shown in Figure S2 and Figure S3, see SI). By using different excitation energies, it is possible to vary the probing depths of the HAXPES measurements. For the Sr 3p and Pb 4f lines, the analyses using 2 and 6 keV result in photoelectron inelastic mean free paths (IMFP) of ≈4 nm and ≈10 nm, respectively (see Methods section for more details on how IMFP relates to probing depth).(34,35)Figure 2a shows that the [Sr]:[Pb] ratios computed from the 6 keV (i.e., more bulk-sensitive) HAXPES measurements are in quite good agreement with the nominal concentrations. However, the [Sr]:[Pb] ratios derived from the 2 keV (i.e., more surface-sensitive) measurements are generally higher and increasingly deviate from the nominal for Sr concentrations ≥0.5%. This trend indicates a Sr rich MAPbI₃ surface with significant Sr surface segregation for 1% and 2% Sr doping.
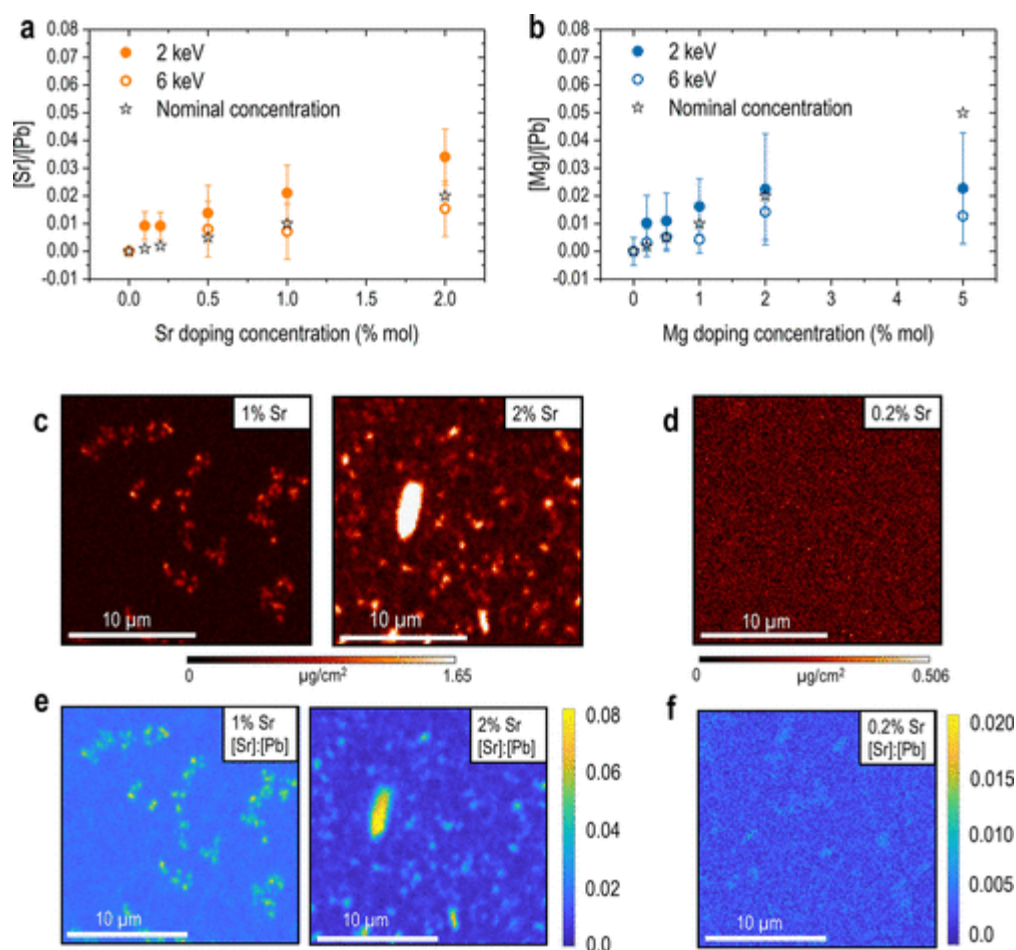
Figure 2

Figure 2. X-ray-based chemical characterizations. (a) Sr and (b) Mg doping levels as determined from the [Sr]:[Pb] and [Mg]:[Pb] ratio derived from the Sr $3p_{3/2}$/Pb $4f_{7/2}$ and Mg 1s/Pb $4f_{7/2}$ hard X-ray photoelectron spectroscopy (HAXPES) data of the investigated sample series measured with 2 and 6 keV. No values are provided for samples for which the dopant signal could not be separated from the spectral background (due to insufficient signal-to-noise ratio and being below the detection limit). Top view of nano X-ray fluorescence (nXRF) elemental concentration maps of (c) 1% and 2% Sr-doped MAPbI₃ thin film and (d) 0.2% Sr-doped MAPbI₃ thin film. The color scale indicates the amount of Sr present in the investigated area in μg/cm². Their corresponding ratio maps between Sr and Pb of (e) 1% and 2% Sr-doped MAPbI₃ thin film and (f) 0.2% Sr-doped MAPbI₃ thin film in which the ratio is presented by the color scale on the right side of the figure.

For the Mg 1s line, the measurements using 2 and 6 keV have IMFP of $\approx$2 nm and $\approx$8 nm, respectively. The calculated [Mg]:[Pb] ratios computed from the 2 and 6 keV measurements mainly agree with the nominal doping concentrations within the experimental uncertainty as can be seen in Figure 2b. However, unlike Sr doping series, the comparison between the two measurements of different probing depths may indicate (if at all present) a less pronounced Mg surface enrichment. The 5% Mg-doped sample is a notable exception. For this sample, the HAXPES derived composition is the same as determined for the 2% Mg-doped MAPbI$_3$ and thus below the nominal doping concentration, which can be an indication for grain boundary accumulation requiring further investigation in our next study.

To further test for the nonuniform distribution profile of dopants at different doping concentration in the perovskite layer, we made use of spatially resolved synchrotron-based nano X-ray fluorescence (nXRF) mapping. nXRF is more bulk-sensitive than HAXPES and offers an opportunity to obtain the lateral elemental distribution within the film. Figure 2c,d shows the surface elemental distribution imaging of the perovskite film at Sr doping levels of 1% together with 2% and 0.2% corresponding to the two different doping regimes that we proposed earlier. The relatively low fluorescence yield of Mg[36] means that its presence at this low concentration cannot be detected by the measurement; hence, only Sr doping series are presented here. With a doping concentration of 1% and even more pronounced in the 2% map (Figure 2c), evidence of segregation as bright feature of Sr-rich phases is observed, similar to reports by Lau et al.[21] and Caprioglio et al.[22] To compare with HAXPES data, we plot ratio maps of [Sr]:[Pb]. Although the average values of [Sr]:[Pb] agree well with the nominal concentration in Figure 2e, the [Sr]:[Pb] is significantly higher in the localized regions (up to 8% in the 2% Sr-doped sample map). These regions of increased Sr content may explain the Sr enrichment suggested by the HAXPES analysis. We cannot detect clear Sr agglomeration for doping level in the low doping regime. The 0.2% sample in Figure 2d shows a reasonably uniform distribution of Sr over the investigated area with approximately 0.2% [Sr]:[Pb] (Figure 2f). The small intensity variation of this particular map is likely due to a slightly inhomogeneous sample, which is corroborated by the Pb map (Figure S5). Thus, we conclude that Sr can be incorporated in the perovskite lattice, but the ability to host Sr saturates at a concentration lower than 1%.

Figure 3a and Figure 3b show the grazing incidence X-ray diffraction (GIXRD) patterns, which confirm the tetragonal phase of MAPbI$_3$ in all the Sr and Mg-doped samples agreeing with the theoretically calculated pattern (Figure 3a).[38] Upon the addition of Sr^{2+} and Mg^{2+}, no new peaks are detected, which indicates that no new crystalline phases are formed (although signals from the ITO substrate and PbI$_2$ are present in some cases; see SI for the related discussion). Thus, GIXRD does not detect any secondary phase segregated at the sample surface (as suggested by nXRF and HAXPES data of the highly Sr-doped MAPbI$_3$ samples, see Figure 2), suggesting that the surface phase is amorphous or too thin/too dispersed to be detected by GIXRD. (The GIXRD detection limit for the used setup is estimated to be 0.5% of the probed volume.) Nonetheless, foreign cations may still be incorporated into the perovskite lattice. To detect if any inclusion occurred, we conducted a Le Bail refinement of the GIXRD patterns (fits are reported in Figure S6a and Figure S23, SI)[39] to characterize the microstrain due to doping. The effect of crystallite size broadening is also included in the refinement (see Methods section for more details). The contributions on the peak broadening from microstrain and crystallite size are further graphically shown in Williamson–Hall plots (Figure S6b, SI).
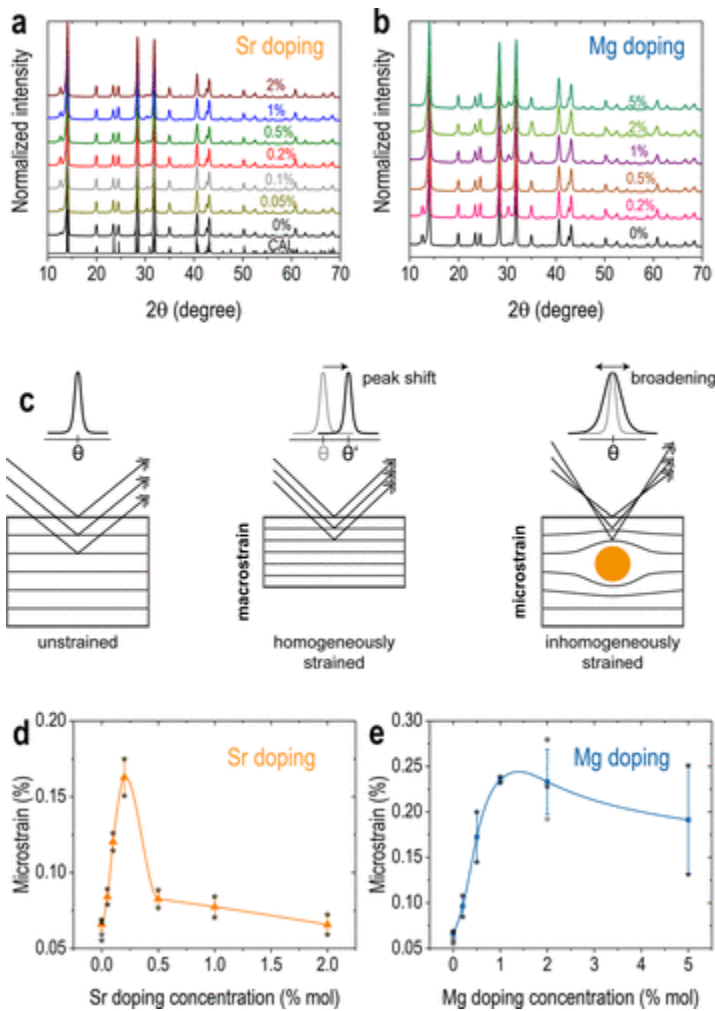
Figure 3

Figure 3. Structural characterization. Grazing incidence X-ray diffraction (XRD) patterns of (a) Sr doping series (including the theoretical calculation of MAPbI$_3$) and (b) Mg doping series. (c) Schematic of macrostrain, which causes a peak shift in XRD pattern, and microstrain, which causes peak broadening (illustration adapted from ref (37)). Microstrain values obtained by Le Bail refinement of (d) the Sr doped MAPbI$_3$ and (e) the Mg-doped MAPbI$_3$ sample series as a function of nominal dopant concentration. The depicted microstrain values are the mean of at least two different samples (individual values are shown in star points next to the mean values), and the stated error bar represents the standard deviation. Spline fits of the values are shown as a guide for visual clarification.

As schematically shown in Figure 3c, the microstrain represents a local distortion of the lattice, which can be detected as a broadening of the peaks. There are no systematic shifts of the XRD peaks (focused and overlapped patterns are shown in Figure S6c,d) indicating the absence of lattice macrostrain or homogeneous changes in the crystal structure. Due to the low concentration of dopants, which can be included in the perovskite lattice, the small number of doped unit cells compared to the coherent domain can only be shown by the microstrain or inhomogeneous strain. The microstrain evolution of the Sr (Figure 3d) and Mg (Figure 3e) doping series shows that the perovskite phase exhibits increasing lattice distortion up to a specific doping level, above which the lattice relaxes back when the segregation of the second phase starts. In particular, the microstrain of Sr-doped samples reaches a maximum value at 0.2% and quickly drops at higher concentrations, where segregation dominates the doping process (see HAXPES and nXRF data related discussion in conjunction with Figure 2 above). The microstrain at this high doping regime, specifically 2%, declines to a value of 0.07%, similar to the undoped sample's level. As is clearly evident from Figure S6e, the lattice parameters of MAPbI$_3$ change upon Sr doping in both directions of the tetragonal unit cell implying lattice inclusion. Therefore, we have strong evidence that at 0.2% Sr doping concentration, the dopant can be incorporated into the perovskite lattice. As can be seen in Figure 2, HAXPES and nXRF have different probing volumes, but derived ratios are similar within the uncertainty (1±0.5% and 0.2% respectively). Thus, this [Sr]:[Pb] ratio can give an indication of the amount of Sr in the perovskite crystal, which is less than 1%. However, we acknowledge that a precise amount of Sr requires a further investigation in a follow up study.

In the Mg doping series, the microstrain shows a more gradual decrease after the maximum is reached at 1% doping concentration. This might indicate that lattice incorporation and lattice relaxation due to segregation can happen simultaneously at concentrations higher than 1%. This is in agreement with the HAXPES derived conclusion of a less pronounced Mg surface segregation. Hence, Mg doping can have a higher threshold until the surface segregation occurs. Noticeably, the most significant microstrain occurs at a higher doping concentration in the case of Mg (1%) than in the case of Sr (0.2%), with higher absolute values in the Mg case. Besides, as can be seen in Figure S6f, the lattice indicates a contraction in the c-direction with the most significant change at 1% Mg, which is different from uniform changes in the Sr-doped perovskite lattice in both directions, shown in Figure S6e. The difference can originate from the smaller ionic radius of Mg^{2+} (72 pm) compared to that of Sr^{2+} (118 pm) and Pb^{2+} (119 pm),(16) which influences the ability to incorporate the doping atom into the perovskite lattice. Notably, our DFT calculations predict very similar Pb–I and Sr–I average bond lengths of 320 and 323 pm in pristine and Sr-doped (substitutional Sr_{Pb}) perovskites, while shorter Mg–I bond of 298 pm is reported in Mg-doped (substitutional Mg_{Pb}) systems, in agreement with the tabulated ionic radii from Shannon et al.(16) The comparison of the microstrain trend in the case of Sr doping with the corresponding HAXPES data in Figure 2 corroborates our hypothesis above that the dopant is incorporated into the perovskite lattice until a critical distortion is reached. Then, the dopant starts to segregate at the surface, resulting in a relaxation of the perovskite lattice.

We investigated how different doping regime influences the position of the valence band maximum (VBM) concerning the E_F using HAXPES. Figure 4a and Figure 4b show the VBM position of the investigated Sr-doped and Mg-doped MAPbI$_3$ sample series, respectively (full spectra and details on VBM determination are shown in Figure S4, SI). Assuming that the bandgap (E_g) at the surface of the sample is the same as its optical E_g (i.e., ≈ 1.6 eV obtained from Tauc plots of corresponding UV–vis spectra shown in Figure S7, SI), the undoped MAPbI$_3$ would exhibit a (slight) n-type character on the sample surface. By adding dopants, similar trends can be detected in the VBM position as a function of dopant concentration for 2 and 6 keV measurements. At low doping levels (i.e., lower than 0.5% Sr- and 2% Mg-doped, indicated by the blue area in Figure 4a and Figure 4b), the films become more n-type compared to the undoped MAPbI$_3$, whereas with higher doping concentration, the VBM shifts closer to E_F, which would be in agreement with a less n-type character. Note that in this doping concentration regime segregated surface phases and—independent of doping concentration—the presence of metallic lead (Pb^0) could also impact the position of the VBM compared to E_F. However, we do not expect either to have a significant impact (see SI for detailed discussion).
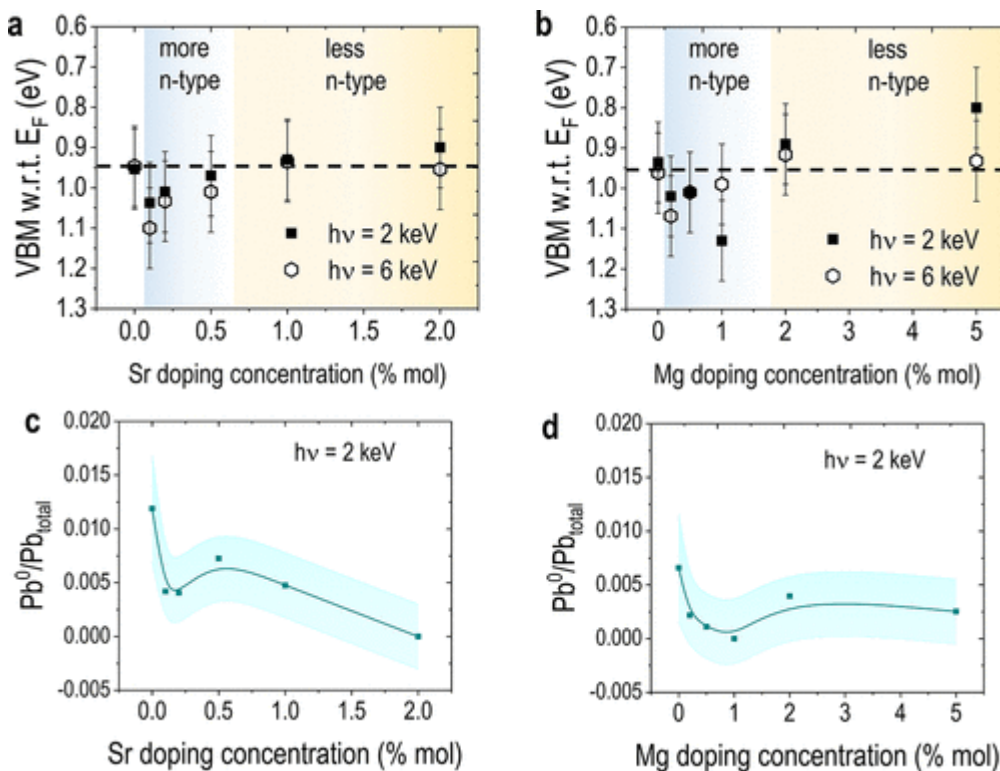
Figure 4

Figure 4. Influence of dopants on electronic properties. Position of the valence band maximum (VBM) of the studied MAPbI$_3$ samples concerning the Fermi level (E_F) for various nominal doping concentrations of (a) Sr and (b) Mg derived from 2 and 6 keV HAXPES data. The region in which the doped perovskite is more n-type compared to the

undoped material is indicated in blue, whereas less n-type region is shown in yellow. The dashed line denotes the value obtained for the undoped samples. The fraction of metallic lead (Pb^0) compared to the total amount of lead at the surface of the samples, as determined by 2 keV HAXPES measurements, is shown in (c) for the Sr and in (d) for the Mg-doped $MAPbI_3$ sample series. The experimental uncertainty is presented as the area along with the corresponding spline fits of the values as a guide for visual clarification.

Notably, even the small changes in absolute Sr concentration from 0.1% Sr to 0.5% Sr-doped causes a VBM shift from 1.04 ± 0.1 eV to 0.97 ± 0.1 eV concerning E_F, tending toward the VBM of the undoped sample. This tendency is similar for 1% and 2% Mg-doped samples. It indicates that different concentration regimes of *one* dopant can vary the n-type doping level. We can correlate the reasons behind this change to the change in defect concentrations of the films as the number of dominant vacancies can induce n or p-doping of perovskite.[31] Together with theoretical calculation (discussed in detail in SI), we postulate that the dopants included in the lattice can passivate Pb (V_{Pb}^{2-}) and MA (V_{MA}^-) vacancies. This can result in a more n-type material, whereas less n-type doping might be realized by the increase in iodine interstitials (I_i^-) due to the iodine excess in the precursors in this case. The DFT calculation shows that the V_{Pb}^{2-} passivation is favored by 0.24 and 0.11 eV for Sr^{2+} and Mg^{2+}, respectively. This scenario would be in agreement with the significant reduction of the Pb^0 content in the sample upon doping shown in Figure 4c and Figure 4d. After Pb^{2+} site is saturated with Sr^{2+} and Mg^{2+}, the n-type doping can further be a result of V_{MA}^- passivation with the formation energy of −0.44 and 0.01 eV, respectively. Furthermore, since Mg^{2+} has a higher inclusion concentration than Sr^{2+} despite its unfavorable tolerance factor to form 3D MA-based perovskite, it indicates a plausible scenario of Mg^{2+} included stably in interstitial position.

Device Performance

To study the impact of the dopants on the performance of complete solar cells, we prepared p-i-n devices made of ITO/PTAA/$MAPbI_3$/C_{60}/BCP/Cu, as previously reported (see Methods section).[41] Figure 5a,b display the device's open circuit voltage (V_{OC}) as a function of the doping level for Sr and Mg (full set of parameters are presented in Figure S13, SI). Remarkably, the microstrain of the perovskite lattice reported in Figure 3, which we replotted here, follows the V_{OC} trend. In particular, we observe a maximum in both microstrain and V_{OC} at 0.2% Sr- and 1% Mg-doped devices, and a (slight) decrease after the maximum has been reached. It is worth noticing that at high Sr doping levels (more than 0.5% Sr), the microstrain decreases to the undoped level, yet V_{OC} is still improved compared to undoped devices. This can be attributed to possible surface passivation by the Sr surface phase segregation also seen in the literature.[20,22]

Figure 5
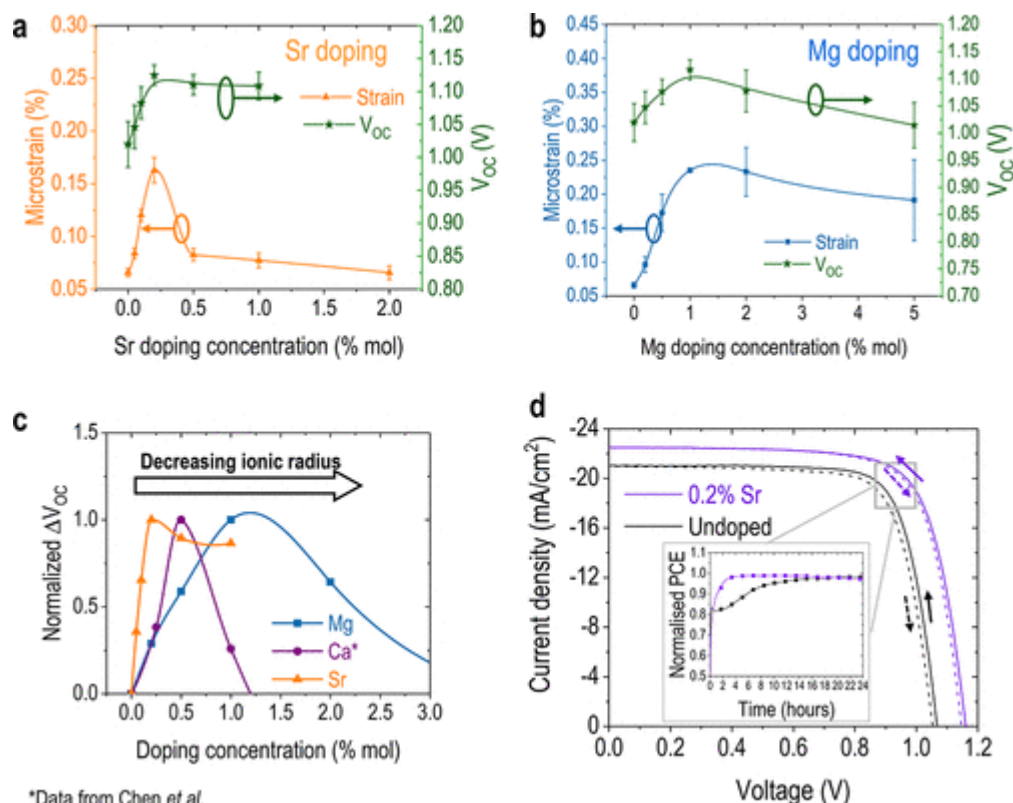
*Data from Chen et al.

Figure 5. Device performance upon doping. Correlation between open circuit voltage (V_{OC}) of solar cell devices with microstrain from GIXRD refinement of (a) the Sr-doped MAPbI$_3$ series and (b) the Mg-doped MAPbI$_3$ series. (c) Open circuit voltage trend with respect to nominal doping concentration of 3 alkaline earth metal ions, namely, Mg^{2+}, Ca^{2+}, and Sr^{2+} (data for Ca^{2+} doping is collected from Chen et al.)[40] (d) Current density–voltage (J–V) curve of the best 0.2% Sr-doped with antireflection coating and undoped MAPbI$_3$ device measured at standard AM1.5 1 sun equivalent condition with a 100 mV/s scan rate. Arrows indicate scan direction. The inset is continuous maximum power point tracking in N$_2$ at 25 °C, in simulated global AM1.5 solar spectrum with UV cut-off at 380 nm for 24 h.

This similar trend between V_{OC} and microstrain indicates the positive impact of lattice incorporation of the dopants to reduce defect concentration in MAPbI$_3$. As mentioned in the previous section, the DFT calculations predict defect passivation by incorporating Sr^{2+} and Mg^{2+} (see SI for details), which can explain the high V_{OC} with lattice incorporation of the dopants. We further calculated quasi-Fermi level splitting of perovskite layer and reinforced that the voltage improvement stems from bulk defect passivation rather than interfacial passivation at low doping concentration (see Figure S14 and related discussion in SI). Furthermore, we extend the analysis of the V_{OC} trend to literature data to include Ca into the series of dopants. The data points of CaI$_2$ doping are plotted from Chen et al. with similar doping concentration range.[40]Figure 5c shows the relative change in V_{OC} of Mg^{2+}, Ca^{2+}, and Sr^{2+} doped devices as a function of doping concentration. Although the trend of V_{OC} is similar for all three dopants, the highest V_{OC} occurs at 1% for Mg, 0.5% for Ca,[40] and 0.2% for Sr doping. Interestingly, this trend corresponds to the pattern of effective radii of the dopants as well (Mg^{2+} (72 pm) < Ca^{2+} (100 pm) < Sr^{2+} (118 pm)).[16] Thus, the highest V_{OC} happens at a higher doping concentration for dopants with smaller ionic radii, which implies that the ability to host dopants in MAPbI$_3$ depends on the radii of the dopants.

The low doping regime where the dopants can be included in the perovskite lattice and passivate defects results in better device performance. In particular, upon Sr and Mg doping, the average V_{OC} improves by about 100 mV (from 1023 mV on average for undoped devices to more than 1117 mV and 1125 mV on average for Sr-doped and Mg-doped devices, respectively). Full PV parameters are shown in Figure S13. Figure 5d displays the champion p-i-n MAPbI$_3$ device with 0.2% Sr doping, which shows short circuit current density (J_{SC}) of 22.5 mA/cm^2 (in agreement with integrated current density from external quantum efficiency plot in Figure S17b), fill factor (FF) of 74.3% and a V_{OC} of 1161 mV, resulting in an efficiency of 19.4% (stabilized at 19%) compared to 17.2% of the best undoped MAPbI$_3$ device. To further prove the effectiveness of low doping regime, n-i-p 0.2% Sr-doped MAPbI$_3$ devices were fabricated, resulting in a more than 20% champion device compared to 18.7% of undoped MAPbI$_3$ device shown in Figure S19. The long-term stability of the doped MAPbI$_3$ compared to undoped MAPbI$_3$ is shown in the inset Figure 5d. The transient of the first few hours is suppressed by doping. The Sr-doped device shows a quick transient reaching its maximum power output in 2 h, whereas it takes more than 20 h for the undoped device to reach the stabilized PCE. This trend might be attributed to faster ion migration[42] or a reduction of the number of mobile ionic defects upon doping.

Conclusion

In this study, we investigated the doping mechanism of halide perovskites using Sr^{2+} and Mg^{2+} to compare doping elements with similar chemical properties but different ionic radii. We found two distinct doping regimes. The low doping concentration regime, which results in incorporation of the dopant into the perovskite lattice, and the high doping concentration regime, which results in surface phase segregation. We observed that the threshold between the low and the high doping regimes depends on the size of the doping element. In particular, methylammonium lead iodide perovskite can incorporate a larger quantity of Mg^{2+} than Sr^{2+}due to their difference in ionic radius. We discussed the impact of the dopant incorporation and the surface segregation on the n-type character of the materials as the result of the interaction of the doping element with the defect chemistry of the material. Thus, we prove the effectiveness of the low doping regime for the first time, demonstrating MAPbI$_3$ based solar cells with an open circuit voltage exceeding 1.16 V and stabilized PCE of more than 19% for p-i-n structure and more than 20% PCE for n-i-p solar cells. Our work provides a comprehensive picture of the doping mechanism of halide perovskites semiconductor, which is somewhat different from doping of classical semiconductors.

Methods

Solar Cells Fabrication

All chemicals are used as received. The perovskite solution is mixed from 1.2 M of PbI$_2$ (Tokyo Chemical Industry), and CH$_3$NH$_3$I (Dyenamo) in mixed solvent DMF:DMSO 6:1 (v:v). The dopant SrI$_2$ (Alfa Aesar) is dissolved in DMSO (1 M) and MgI$_2$ (Santa Cruz) is dissolved in DMF:DMSO 6:1 (0.7 M). The amount of dopants in the perovskite solution is calculated according to the molar ratio with PbI$_2$. The final perovskite solution is shaken at 60 °C for 5 min to dissolve all components.

In-doped SnO$_2$ (ITO) substrates (Automatic Research, 15 Ω·cm^{-2}) are sonicated for 15 min with Mucasol (2% in deionized water), acetone and isopropyl for cleaning and eventually UV-ozone treatment for 15 min. Prior to perovskite deposition, PTAA (poly[bis(4-phenyl)(2,4,6-trimethylphenyl)amine]) (Sigma-Aldrich) with a concentration of 2 mg/mL in toluene is spin-coated on clean substrates (4000 rpm for 30 s). The substrate is then annealed at 100 °C for 10 min. 100 μL of perovskite solution is dropped on room temperature substrate before starting the spin coating program (4000 rpm for 30 s, ramping for 5 s). After 20 s of spin coating, 500 μL of ethyl acetate is dropped on the substrate to form a smooth and compact film. The perovskite film is immediately annealed at 100 °C for 60 min. Finally, C$_{60}$ (20 nm) (Sigma-Aldrich), BCP (bathocuproine or 2,9-Dimethyl-4,7-diphenyl-1) (10 nm) (Sigma-Aldrich), and Cu (100 nm) (Alfa Aesar, 99.95% purity) are evaporated on the perovskite layer to complete the device. All of these fabrication steps are done in an inert atmosphere with minimized air exposure.

For n-i-p MAPbI$_3$, the compact TiO$_2$ is deposited on cleaned F-doped SnO$_2$ (FTO, 15 Ω·cm^{-2}) using a method reported elsewhere.[43] In short, the cleaned FTO substrates are submerged in 200 mL TiCl$_4$ solution at 70 °C for 1 h, then the substrates are cleaned thoroughly with deionized water and dried at 100 °C for 1 h. The TiO$_2$ layer is treated with UV-ozone for 30 min before perovskite deposition. The hole selective layer is prepared as followed. 36.15 mg of Spiro-OMETAD is dissolved in 1 mL of chlorobenzene, then 14.40 μL 4-*tert*-Butylpyridine (Sigma-Aldrich, 98%), 8.75 μL of Li-TFSI (bis(trifluoromethane)sulfonimide lithium salt, 99.95% trace metals basis, Sigma-Aldrich) (300 mg per mL of acetonitrile), and 14.50 μL FK209 (Co(II) salt, Sigma-Aldrich) (500 mg per mL of acetonitrile) are added to the Spiro-OMETAD solution. Finally, 80 nm of Au (Alfa Aesar, 99.99% purity) is evaporated on top to finish the device.

Hard X-ray Photoelectron Spectroscopy

Hard X-ray photoelectron spectroscopy (HAXPES) measurements were carried out at the HiKE endstation located at the BESSY II KMC-1 beamline at Helmholtz-Zentrum Berlin (HZB).[44,45] The HiKE endstation is equipped with a Scienta R4000 electron analyzer and an excitation energy of 2003 eV (referred to as "2 keV") and 6009 eV (referred to as "6 keV") were employed. The binding energy (BE) scale of the HAXPES measurements was calibrated by measuring the Au 4f energy region of a clean Au foil in electrical contact with the (grounded) sample and setting the BE of the Au 4f$_{7/2}$ line to 84.0 eV. The pressure in the endstation's analysis chamber during the HAXPES measurements remained <1 × 10^{-8} mbar. Curve fit analysis of measured detail HAXPES spectra were simultaneously conducted using the Fityk software.[46] Voigt profile functions, along with linear backgrounds, were employed for these fits. Spin–orbit doublets were fitted using two Voigt functions with intensity ratios set to obey the $2j + 1$ multiplicity rule. The peak intensities of the HAXPES core levels were corrected to account for differences in photoionization cross section (σ),[47−49] and when required also for changes in the inelastic mean free path (IMFP),[34,35] and the transmission function of the electron analyzer (T).[50] To quantify the Pb 4f spectra, two doublet peak pairs were used to account for the core level contributions and five additional (broader) pairs to account for the satellites' contribution background (derived from electron energy losses related to valence and conduction band transitions in PbX$_2$ systems).[51,52] The Sr 3p signal can be detected in all the Sr doped samples, whereas the Sr 3d signal is only absent for the lowest (0.1%) Sr-doped sample. This apparent difference can be explained by two factors: First, at 2 keV excitation, the σ for the Sr 3p core levels are approximately three times higher than that of Sr 3d core levels in our experimental setup.[47] Moreover, in contrast to the Sr 3p core levels, which have a linear background, the Sr 3d core levels directly overlap with the Pb 4f$_{7/2}$ line, the most prominent Pb-related photoelectron line at the used excitation energy, which explains why the Sr 3d signal is below the detection limit at low Sr concentrations (i.e., 0.1% doping). For these reasons, although the close energetic proximity of the Pb 4f/Sr 3d core levels would present a straightforward opportunity to quantify the [Sr]:[Pb] ratios just by normalizing the signal of each core level by its corresponding σ,[47] we chose to calculate the [Sr]:[Pb] ratios from the more prominent core lines (i.e., Sr 3p$_{3/2}$ and Pb 4f$_{7/2}$). The HAXPES probing depth is governed by the IMFP of the probed photoelectrons. The main contribution stems from the surface of the sample, which decays exponentially to 1/e within IMFP. For the Sr 3p and Pb 4f lines, the measurements using 2 and 6 keV have an IMFP of ≈4 nm and ≈10 nm, respectively.[48,49] For the Mg 1s line, the measurements using 2 and 6 keV have IMFP values of ≈2 nm and ≈8 nm, respectively.[48,49] The position of the valence band maximum (VBM) with respect to the Fermi level (E_F) was determined by linear approximation of the leading edge of the valence band spectra shown in Figure S4.

Nano X-ray Fluorescence

The synchrotron-based nano X-ray fluorescence (nXRF) measurements for the elemental mapping of the perovskite films were done in the 2-ID-D beamline at an excitation energy of 16 keV, X-ray step size of 0.15 μm, and a dwell time of 50 ms at the Advanced Photon Source, Argonne National Laboratory. The MAPS software, written in IDL programming language, was used to display the acquired XRF data. Because Sr is commonly found in glass substrates (e.g., the used ITO-coated glass substrate), the perovskite films employed in the nXRF analysis were prepared on quartz substrates, following the same procedure detailed in the Solar Cells Fabrication subsection above. The purpose of the

measurement is to check the possibility of two doping regimes. We chose 0.2%, 1%, and 2% to have at least 1 order of magnitude difference in doping concentration for the two regimes.

Density Functional Theory Calculations

Density functional theory (DFT) calculations have been carried out by modeling defects in the $2 \times 2 \times 2$ supercell of MAPbI$_3$, by fixing cell parameters to the experimental values.(53) Energies of formation and reaction of Sr and Mg related defects have been calculated by using the Perdew–Burke–Ernzherof (PBE)(54) exchange-correlation functional and ultrasoft pseudopotentials with a cutoff on the wave functions of 40 Ryd (320 Ryd on the charge density) sampling the Brillouin zone (BZ) at the Gamma point. Defects formation energies diagrams of Sr and Mg defects in MAPbI$_3$ (Figure S9) have been calculated at the PBE level by following a widely used approach and by simulating I-medium conditions of growth of the perovskite.(55,56) The chemical potentials of Sr and Mg have been calculated by imposing the equilibrium with the relative precursors, i.e., $\mu(Mg/Sr) = \mu(MgI_2/SrI_2) – 2\mu(I)$, where $\mu(I)$ is calculated in I-medium conditions and is set according to thermodynamic equilibrium between MAPbI$_3$ and PbI$_2$.

Thermodynamic ionization levels in Figure S8 and the plots of Kohn–Sham orbitals have been calculated by performing single point calculations at the HSE06-SOC(57) level of theory (exchange fraction $\alpha = 0.43$, dispersion included a posteriori through the DFT-D3 scheme(58)) on the equilibrium geometries found at the PBE level.(56) Hybrid calculations have been performed by using norm conserving pseudopotentials with an energy cutoff of 40 Ryd on the wave functions and by sampling the BZ at the Gamma point.(56)

Grazing Incident X-ray Diffraction

The measurement is conducted in air with the PANalytical X'Pert Pro MPD (multipurpose diffractometer) using grazing incidence geometry. Grazing incident X-ray diffraction (GIXRD) patterns are collected with a step size of 0.02 degree, for 10 s each step. On the basis of the signal-to-noise ratio of the collected GIXRD data, we estimate a detection limit of 0.5% crystalline phase in the probed volume.

The Le Bail method was chosen instead of the Rietveld refinement method due to the ease in the calculation without a requirement of the exact atomic positions and the scattering power of the atoms, hence reducing the computation effort.(39) The refinement is done with the FULLPROF program. Here, we could use the full line profile analysis because our XRD patterns show all theoretically predicted peaks from the lattice structure of the material. Different from the standard material, in the polycrystalline film, the XRD peaks can be described by pseudo-Voigt functions. The function is used to consider both Gaussian and Lorentzian contribution to the shape of the peaks in the pattern. Hence, we assume that the angular dependence microstrain will affect to Gaussian peak broadening contribution (the case of Lorentzian contribution to microstrain is rare, so it was excluded from the analysis), whereas the broadening due to crystallite size is from Lorentzian contribution.(59) From this Gaussian contribution, the microstrain is calculated. More details on the refinement can be found in the SI.

Photoluminescence Characterization

Absolute photoluminescence (PL) spectra were recorded from hyperspectral images with a custom setup described elsewhere.(60) We used two 450 nm LEDs for excitation whose fluence are calibrated to 1 sun equivalent and a calibrated CCD camera was used to collect PL emission, coupled to a tunable liquid crystal filter. The setup was calibrated to absolute photon numbers with light sources of known fluences,(61) thus enabling to estimate the quasi Fermi-level splitting (QFLS) from the generalized Planck law using the high-energy tail fit method of the PL spectra.(62)

Current Density–Voltage Measurement

The *J–V* measurement is done with 1 sun equivalent illumination from an Oriel LCS-100 class ABB solar simulator in an inert atmosphere without cooling. The device's active area is 0.16 cm^2. The lamp is calibrated with a Silicon 1 cm^2 diode certified by Fraunhofer ISE.

External Quantum Efficiency (EQE) Measurement

The EQE is measured with a Newport 300 W xenon arc lamp using TracQ software in an Oriel Instruments QEPVSI-b system. A Newport Cornerstone 260 monochromator is used to create monochromatic light chopped at a frequency of 78 Hz. Before the measurement, the system is calibrated with a silicon reference cell with a known spectral response. The electrical response of the device is recorded with a Stanford Research SR830 Lock-In amplifier and evaluated using TracQ.

Ultraviolet–Visible Spectrophotometry

Transmittance and reflectance of the samples are measured with a PerkinElmer Lambda 1050 spectrophotometer equipped with a tungsten-halogen lamp. The measurement is done with a wavelength range of 300 to 850 nm. The derived optical bandgap from the Tauc plot of a direct bandgap material (relation between $(\alpha h\nu)^2$ and $h\nu$) is the intercept between the linear approximation of the absorption edge with the background.

Scanning Electron Microscopy

The images are collected with Hitachi S-4100 at 5 kV acceleration voltage and 30k magnification to obtain top view and cross sectional images.

Supporting Information

The Supporting Information is available free of charge at https://pubs.acs.org/doi/10.1021/jacs.9b11637.

- Full HAXPES spectra of investigated energies; Top view of nXRF; More information on XRD; Details of DFT calculation; Photovoltaic parameters of solar cells; SEM images; PL measurement (PDF)

Terms & Conditions

Author Information

Corresponding Author

- o **Antonio Abate** - *Helmholtz-Zentrum Berlin für Materialien und Energie GmbH, Hahn-Meitner-Platz 1, 14109 Berlin, Germany*; *Department of Chemical, Materials and Production Engineering, University of Naples Federico II, Piazzale Tecchio 80, 80125 Fuorigrotta, Italy*; http://orcid.org/0000-0002-3012-3541; Email: antonio.abate@helmholtz-berlin.de antonio.abate@unina.it

Authors

- o **Nga Phung** - *Helmholtz-Zentrum Berlin für Materialien und Energie GmbH, Hahn-Meitner-Platz 1, 14109 Berlin, Germany*; http://orcid.org/0000-0002-0328-6791

- o **Roberto Félix** - *Helmholtz-Zentrum Berlin für Materialien und Energie GmbH, Hahn-Meitner-Platz 1, 14109 Berlin, Germany*; http://orcid.org/0000-0002-3620-9899

- o **Daniele Meggiolaro** - *Computational Laboratory for Hybrid/Organic Photovoltaics (CLHYO), CNR-ISTM, Via Elce di Sotto 8, 06123 Perugia, Italy*; *D3-CompuNet, Istituto Italiano di Tecnologia, Via Morego 30, 16163 Genova, Italy*; http://orcid.org/0000-0001-9717-133X

- o **Amran Al-Ashouri** - *Helmholtz-Zentrum Berlin für Materialien und Energie GmbH, Hahn-Meitner-Platz 1, 14109 Berlin, Germany*; http://orcid.org/0000-0001-5512-8034

- o **Gabrielle Sousa e Silva** - *Helmholtz-Zentrum Berlin für Materialien und Energie GmbH, Hahn-Meitner-Platz 1, 14109 Berlin, Germany*

- o **Claudia Hartmann** - *Helmholtz-Zentrum Berlin für Materialien und Energie GmbH, Hahn-Meitner-Platz 1, 14109 Berlin, Germany*; http://orcid.org/0000-0002-8017-8161

- o **Juanita Hidalgo** - *School of Materials Science and Engineering, Georgia Institute of Technology, North Avenue NW, Atlanta, Georgia 30332, United States*

- o **Hans Köbler** - *Helmholtz-Zentrum Berlin für Materialien und Energie GmbH, Hahn-Meitner-Platz 1, 14109 Berlin, Germany*

o **Edoardo Mosconi** - *Computational Laboratory for Hybrid/Organic Photovoltaics (CLHYO), CNR-ISTM, Via Elce di Sotto 8, 06123 Perugia, Italy*; *D3-CompuNet, Istituto Italiano di Tecnologia, Via Morego 30, 16163 Genova, Italy*

o **Barry Lai** - *Advanced Photon Source, Argonne National Lab, 9700 Cass Avenue, Lemont, Illinois 60439, United States*

o **Rene Gunder** - *Helmholtz-Zentrum Berlin für Materialien und Energie GmbH, Hahn-Meitner-Platz 1, 14109 Berlin, Germany*

o **Meng Li** - *Helmholtz-Zentrum Berlin für Materialien und Energie GmbH, Hahn-Meitner-Platz 1, 14109 Berlin, Germany*; *Institute of Functional Nano & Soft Materials (FUNSOM), Jiangsu Key Laboratory for Carbon-Based Functional Materials & Devices, Joint International Research Laboratory of Carbon-Based Functional Materials and Devices, Soochow University, Suzhou 215123, PR China*; *Laboratory of Advanced Optoelectronic Materials, College of Chemistry, Chemical Engineering and Materials Science, Soochow University, Suzhou 215123, PR China*

o **Kai-Li Wang** - *Institute of Functional Nano & Soft Materials (FUNSOM), Jiangsu Key Laboratory for Carbon-Based Functional Materials & Devices, Joint International Research Laboratory of Carbon-Based Functional Materials and Devices, Soochow University, Suzhou 215123, PR China*

o **Zhao-Kui Wang** - *Institute of Functional Nano & Soft Materials (FUNSOM), Jiangsu Key Laboratory for Carbon-Based Functional Materials & Devices, Joint International Research Laboratory of Carbon-Based Functional Materials and Devices, Soochow University, Suzhou 215123, PR China*; http://orcid.org/0000-0003-1707-499X

o **Kaiqi Nie** - *Helmholtz-Zentrum Berlin für Materialien und Energie GmbH, Hahn-Meitner-Platz 1, 14109 Berlin, Germany*; *Institute of Functional Nano & Soft Materials (FUNSOM), Jiangsu Key Laboratory for Carbon-Based Functional Materials & Devices, Joint International Research Laboratory of Carbon-Based Functional Materials and Devices, Soochow University, Suzhou 215123, PR China*

o **Evelyn Handick** - *Helmholtz-Zentrum Berlin für Materialien und Energie GmbH, Hahn-Meitner-Platz 1, 14109 Berlin, Germany*; http://orcid.org/0000-0002-9773-9981

o **Regan G. Wilks** - *Helmholtz-Zentrum Berlin für Materialien und Energie GmbH, Hahn-Meitner-Platz 1, 14109 Berlin, Germany*

o **Jose A. Marquez** - *Helmholtz-Zentrum Berlin für Materialien und Energie GmbH, Hahn-Meitner-Platz 1, 14109 Berlin, Germany*; http://orcid.org/0000-0002-8173-2566

o **Bernd Rech** - *Helmholtz-Zentrum Berlin für Materialien und Energie GmbH, Hahn-Meitner-Platz 1, 14109 Berlin, Germany*; *Faculty of Electrical Engineering and Computer Science, Technical University Berlin, Marchstraße 23, 10587 Berlin, Germany*

o **Thomas Unold** - *Helmholtz-Zentrum Berlin für Materialien und Energie GmbH, Hahn-Meitner-Platz 1, 14109 Berlin, Germany*; http://orcid.org/0000-0002-5750-0693

o **Juan-Pablo Correa-Baena** - *School of Materials Science and Engineering, Georgia Institute of Technology, North Avenue NW, Atlanta, Georgia 30332, United States*; http://orcid.org/0000-0002-3860-1149

o **Steve Albrecht** - *Helmholtz-Zentrum Berlin für Materialien und Energie GmbH, Hahn-Meitner-Platz 1, 14109 Berlin, Germany*; *Faculty of Electrical Engineering and Computer Science, Technical University Berlin, Marchstraße 23, 10587 Berlin, Germany*

o **Filippo De Angelis** - *Computational Laboratory for Hybrid/Organic Photovoltaics (CLHYO), CNR-ISTM, Via Elce di Sotto 8, 06123 Perugia, Italy*; *D3-CompuNet, Istituto Italiano di Tecnologia, Via Morego 30, 16163 Genova, Italy*; *Department of Chemistry, Biology and Biotechnology, University of Perugia, Via Elce di Sotto 8, 06123 Perugia, Italy*; http://orcid.org/0000-0003-3833-1975

o **Marcus Bär** - *Helmholtz-Zentrum Berlin für Materialien und Energie GmbH, Hahn-Meitner-Platz 1, 14109 Berlin, Germany*; *Department of Chemistry and Pharmacy, Friedrich-Alexander-Universität Erlangen-Nürnberg, Egerland Str. 3, 91058 Erlangen, Germany*; *Helmholtz Institute Erlangen-Nürnberg for Renewable Energy (HI ERN), Albert-Einstein-Str. 15, 12489 Berlin, Germany*; http://orcid.org/0000-0001-8581-0691

Author Contributions

NP and RF contributed equally to this work.

Notes

The authors declare no competing financial interest.

Acknowledgments

References

This article references 62 other publications.

1. NREL PV Efficiency Chart. https://www.nrel.gov/pv/assets/pdfs/pv-efficiency-chart.20181221.pdf (accessed 02/10/2019).

2. Klug, M. T.; Osherov, A.; Haghighirad, A. A.; Stranks, S. D.; Brown, P. R.; Bai, S.; Wang, J. T.-W.; Dang, X.; Bulović, V.; Snaith, H. J.; Belcher, A. M. Tailoring metal halide perovskites through metal substitution: influence on photovoltaic and material properties. *Energy Environ. Sci.* **2017**, *10* (1), 236– 246, DOI: 10.1039/C6EE03201J

3. Saidaminov, M. I.; Kim, J.; Jain, A.; Quintero-Bermudez, R.; Tan, H.; Long, G.; Tan, F.; Johnston, A.; Zhao, Y.; Voznyy, O.Suppression of atomic vacancies via incorporation of isovalent small ions to increase the stability of halide perovskite solar cells in ambient air. *Nat. Energy* **2018**, *3* (8), 648, DOI: 10.1038/s41560-018-0192-2

4. Zheng, X.; Troughton, J.; Gasparini, N.; Lin, Y.; Wei, M.; Hou, Y.; Liu, J.; Song, K.; Chen, Z.; Yang, C.; Turedi, B.; Alsalloum, A. Y.; Pan, J.; Chen, J.; Zhumekenov, A. A.; Anthopoulos, T. D.; Han, Y.; Baran, D.; Mohammed, O. F.; Sargent, E. H.; Bakr, O. M. Quantum Dots Supply Bulk-and Surface-Passivation Agents for Efficient and Stable Perovskite Solar Cells. *Joule* **2019**, *3*, 1963, DOI: 10.1016/j.joule.2019.05.005

5. Begum, R.; Parida, M. R.; Abdelhady, A. L.; Murali, B.; Alyami, N. M.; Ahmed, G. H.; Hedhili, M. N.; Bakr, O. M.; Mohammed, O. F. Engineering interfacial charge transfer in $CsPbBr_3$ perovskite nanocrystals by heterovalent doping. *J. Am. Chem. Soc.* **2017**, *139* (2), 731– 737, DOI: 10.1021/jacs.6b09575

6. Saliba, M.; Matsui, T.; Domanski, K.; Seo, J.-Y.; Ummadisingu, A.; Zakeeruddin, S. M.; Correa-Baena, J.-P.; Tress, W. R.; Abate, A.; Hagfeldt, A.; Gratzel, M. Incorporation of rubidium cations into perovskite solar cells improves photovoltaic performance. *Science* **2016**, *354* (6309), 206– 209, DOI: 10.1126/science.aah5557

7. Kubicki, D. J.; Prochowicz, D.; Hofstetter, A.; Zakeeruddin, S. M.; Grätzel, M.; Emsley, L. Phase Segregation in Cs-, Rb-and K-Doped Mixed-Cation (MA)x(FA)1–xPbI$_3$ Hybrid Perovskites from Solid-State NMR. *J. Am. Chem. Soc.* **2017**, *139* (40), 14173– 14180, DOI: 10.1021/jacs.7b07223

8. Zhou, Y.; Chen, J.; Bakr, O. M.; Sun, H.-T. Metal-doped lead halide perovskites: synthesis, properties, and optoelectronic applications. *Chem. Mater.* **2018**, *30* (19), 6589– 6613, DOI: 10.1021/acs.chemmater.8b02989

9. Navas, J.; Sánchez-Coronilla, A.; Gallardo, J. J.; Hernández, N. C.; Piñero, J. C.; Alcántara, R.; Fernández-Lorenzo, C.; Desireé, M.; Aguilar, T.; Martín-Calleja, J. New insights into organic–inorganic hybrid perovskite CH$_3$NH$_3$PbI$_3$ nanoparticles. An experimental and theoretical study of doping in Pb^{2+} sites with Sn^{2+}, Sr^{2+}, Cd^{2+} and Ca^{2+}. *Nanoscale* **2015**, *7* (14), 6216– 6229, DOI: 10.1039/C5NR00041F

10. Jacobsson, T. J.; Pazoki, M.; Hagfeldt, A.; Edvinsson, T. Goldschmidt's rules and strontium replacement in lead halogen perovskite solar cells: theory and preliminary experiments on CH$_3$NH$_3$SrI$_3$. *J. Phys. Chem. C* **2015**, *119* (46), 25673– 25683, DOI: 10.1021/acs.jpcc.5b06436

11. Pazoki, M.; Jacobsson, T. J.; Hagfeldt, A.; Boschloo, G.; Edvinsson, T. Effect of metal cation replacement on the electronic structure of metalorganic halide perovskites: Replacement of lead with alkaline-earth metals. *Phys. Rev. B: Condens. Matter Mater. Phys.* **2016**, *93* (14), 144105, DOI: 10.1103/PhysRevB.93.144105

12. Yang, F.; Kamarudin, M. A.; Kapil, G.; Hirotani, D.; Zhang, P.; Ng, C. H.; Ma, T.; Hayase, S. Magnesium-Doped MAPbI$_3$ Perovskite Layers for Enhanced Photovoltaic Performance in Humid Air Atmosphere. *ACS Appl. Mater. Interfaces* **2018**, *10* (29), 24543– 24548, DOI: 10.1021/acsami.8b06619

13. Huang, Q.; Zou, Y.; Bourelle, S.; Zhai, T.; Wu, T.; Tan, Y.; Li, Y.; Li, J.; Duhm, S.; Song, T.; Wang, L.; Deschler, F.; Sun, B. Suppressing Defect State in CsPbBr3 Perovskite via Magnesium Substitution for Efficient All-Inorganic Light-Emitting Diodes. *Nanoscale Horizons* **2019**, *4*, 924– 932, DOI: 10.1039/C9NH00066F

14. Wang, K.; Liang, Z.; Wang, X.; Cui, X. Lead replacement in CH$_3$NH$_3$PbI$_3$ perovskites. *Advanced Electronic Materials* **2015**, *1* (10), 1500089, DOI: 10.1002/aelm.201500089

15. Shai, X.; Zuo, L.; Sun, P.; Liao, P.; Huang, W.; Yao, E.-P.; Li, H.; Liu, S.; Shen, Y.; Yang, Y.; Wang, M. Efficient planar perovskite solar cells using halide Sr-substituted Pb perovskite. *Nano Energy* **2017**, *36*, 213– 222, DOI: 10.1016/j.nanoen.2017.04.047

16. Shannon, R. D. Revised effective ionic radii and systematic studies of interatomic distances in halides and chalcogenides. *Acta Crystallogr., Sect. A: Cryst. Phys., Diffr., Theor. Gen. Crystallogr.* **1976**, *32* (5), 751– 767, DOI: 10.1107/S0567739476001551

17. Goldschmidt, V. M. Die gesetze der krystallochemie. *Naturwissenschaften* **1926**, *14* (21), 477– 485, DOI: 10.1007/BF01507527

18. Li, Z.; Yang, M.; Park, J.-S.; Wei, S.-H.; Berry, J. J.; Zhu, K. Stabilizing perovskite structures by tuning tolerance factor: formation of formamidinium and cesium lead iodide solid-state alloys. *Chem. Mater.* **2016**, *28* (1), 284– 292, DOI: 10.1021/acs.chemmater.5b04107

19. Kieslich, G.; Sun, S.; Cheetham, A. K. An extended tolerance factor approach for organic–inorganic perovskites. *Chemical science* **2015**, *6* (6), 3430– 3433, DOI: 10.1039/C5SC00961H

20. Pérez-del-Rey, D.; Forgács, D.; Hutter, E. M.; Savenije, T. J.; Nordlund, D.; Schulz, P.; Berry, J. J.; Sessolo, M.; Bolink, H. J. Strontium Insertion in Methylammonium Lead Iodide: Long Charge Carrier Lifetime and High Fill-Factor Solar Cells. *Adv. Mater.* **2016**, *28* (44), 9839– 9845, DOI: 10.1002/adma.201603016

21. Lau, C. F. J.; Zhang, M.; Deng, X.; Zheng, J.; Bing, J.; Ma, Q.; Kim, J.; Hu, L.; Green, M. A.; Huang, S.; Ho-Baillie, A. Strontium-doped low-temperature-processed CsPbI$_2$Br perovskite solar cells. *ACS Energy Letters* **2017**, *2* (10), 2319– 2325, DOI: 10.1021/acsenergylett.7b00751

22. Caprioglio, P.; Zu, F.; Wolff, C. M. M.; Prieto, J. A. M.; Stolterfoht, M.; Becker, P.; Koch, N.; Unold, T.; Rech, B.; Albrecht, S.; Neher, D. High open circuit voltages in pin-type perovskite solar cells through strontium addition. *Sustainable Energy Fuels* **2019**, *3*, 550– 563, DOI: 10.1039/C8SE00509E

23. Walsh, A.; Scanlon, D. O.; Chen, S.; Gong, X.; Wei, S. H. Self-Regulation Mechanism for Charged Point Defects in Hybrid Halide Perovskites. *Angew. Chem., Int. Ed.* **2015**, *54* (6), 1791– 1794, DOI: 10.1002/anie.201409740

24. Ming, W.; Chen, S.; Du, M.-H. Chemical instability leads to unusual chemical-potential-independent defect formation and diffusion in perovskite solar cell material $CH_3NH_3PbI_3$. *J. Mater. Chem. A* **2016**, *4* (43), 16975– 16981, DOI: 10.1039/C6TA07492H

25. Meggiolaro, D.; Motti, S. G.; Mosconi, E.; Barker, A. J.; Ball, J.; Perini, C. A. R.; Deschler, F.; Petrozza, A.; De Angelis, F. Iodine chemistry determines the defect tolerance of lead-halide perovskites. *Energy Environ. Sci.* **2018**, *11* (3), 702– 713, DOI: 10.1039/C8EE00124C

26. Zhang, H.; Li, R.; Zhang, M.; Guo, M. The effect of SrI_2 substitution on perovskite film formation and its photovoltaic properties via two different deposition methods. *Inorg. Chem. Front.* **2018**, *5* (6), 1354– 1364, DOI: 10.1039/C8QI00131F

27. Zhang, H.; Wang, H.; Williams, S. T.; Xiong, D.; Zhang, W.; Chueh, C. C.; Chen, W.; Jen, A. K. Y. $SrCl_2$ Derived Perovskite Facilitating a High Efficiency of 16% in Hole-Conductor-Free Fully Printable Mesoscopic Perovskite Solar Cells. *Adv. Mater.* **2017**, *29* (15), 1606608, DOI: 10.1002/adma.201606608

28. Wu, M.-C.; Chen, W.-C.; Chan, S.-H.; Su, W.-F. The effect of strontium and barium doping on perovskite-structured energy materials for photovoltaic applications. *Appl. Surf. Sci.* **2018**, *429*, 9– 15, DOI: 10.1016/j.apsusc.2017.08.131

29. Würfel, P.; Würfel, U. *Physics of Solar Cells: From Basic Principles to Advanced Concepts*; John Wiley & Sons, 2016.

30. Zhang, S.; Wei, S.-H.; Zunger, A.; Katayama-Yoshida, H. Defect physics of the $CuInSe_2$ chalcopyrite semiconductor. *Phys. Rev. B: Condens. Matter Mater. Phys.* **1998**, *57* (16), 9642, DOI: 10.1103/PhysRevB.57.9642

31. Xiao, Z.; Yuan, Y.; Shao, Y.; Wang, Q.; Dong, Q.; Bi, C.; Sharma, P.; Gruverman, A.; Huang, J. Giant switchable photovoltaic effect in organometal trihalide perovskite devices. *Nat. Mater.* **2015**, *14* (2), 193, DOI: 10.1038/nmat4150

32. Wang, Q.; Shao, Y.; Xie, H.; Lyu, L.; Liu, X.; Gao, Y.; Huang, J. Qualifying composition dependent p and n self-doping in $CH_3NH_3PbI_3$. *Appl. Phys. Lett.* **2014**, *105* (16), 163508, DOI: 10.1063/1.4899051

33. Olthof, S.; Meerholz, K. Substrate-dependent electronic structure and film formation of $MAPbI_3$ perovskites. *Sci. Rep.* **2017**, *7*, 40267, DOI: 10.1038/srep40267

34. Tougaard, S. *QUASES-IMFP-TPP2M program*. Quases-Tougaard Inc., 2002.

35. Tanuma, S.; Powell, C. J.; Penn, D. R. Calculations of electron inelastic mean free paths. V. Data for 14 organic compounds over the 50–2000 eV range. *Surf. Interface Anal.* **1994**, *21* (3), 165– 176, DOI: 10.1002/sia.740210302

36. Mattox, D. M. *Handbook of Physical Vapor Deposition (PVD) Processing*; William Andrew, 2010.

37. Attfield, M.; Barnes, P.; Cockcroft, J. K.; Driessen, H. Crystallite Size and Strain. http://pd.chem.ucl.ac.uk/pdnn/peaks/size.htm (accessed 01/03/2018).

38. Yamada, Y.; Yamada, T.; Phuong, L. Q.; Maruyama, N.; Nishimura, H.; Wakamiya, A.; Murata, Y.; Kanemitsu, Y. Dynamic optical properties of $CH_3NH_3PbI_3$ single crystals as revealed by one-and two-photon excited photoluminescence measurements. *J. Am. Chem. Soc.* **2015**, *137* (33), 10456– 10459, DOI: 10.1021/jacs.5b04503

39. Le Bail, A.; Jouanneaux, A. A Qualitative Account for Anisotropic Broadening in Whole-Powder-Diffraction-Pattern Fitting by Second-Rank Tensors. *J. Appl. Crystallogr.* **1997**, *30* (3), 265– 271, DOI: 10.1107/S0021889896011922

40. Chen, C.; Xu, Y.; Wu, S.; Zhang, S.; Yang, Z.; Zhang, W.; Zhu, H.; Xiong, Z.; Chen, W.; Chen, W. CaI$_2$: a more effective passivator of perovskite films than PbI$_2$ for high efficiency and long-term stability of perovskite solar cells. *J. Mater. Chem. A* **2018**, *6* (17), 7903– 7912, DOI: 10.1039/C7TA11280G

41. Saliba, M.; Correa-Baena, J.-P.; Wolff, C. M.; Stolterfoht, M.; Phung, N.; Albrecht, S.; Neher, D.; Abate, A. How to make over 20% efficient perovskite solar cells in regular (n–i–p) and inverted (p–i–n) architectures. *Chem. Mater.* **2018**, *30* (13), 4193– 4201, DOI: 10.1021/acs.chemmater.8b00136

42. Domanski, K.; Roose, B.; Matsui, T.; Saliba, M.; Turren-Cruz, S.-H.; Correa-Baena, J.-P.; Carmona, C. R.; Richardson, G.; Foster, J. M.; De Angelis, F.; Ball, J. M.; Petrozza, A.; Mine, N.; Nazeeruddin, M. K.; Tress, W.; Grätzel, M.; Steiner, U.; Hagfeldt, A.; Abate, A. Migration of cations induces reversible performance losses over day/night cycling in perovskite solar cells. *Energy Environ. Sci.* **2017**, *10* (2), 604– 613, DOI: 10.1039/C6EE03352K

43. Yella, A.; Heiniger, L.-P.; Gao, P.; Nazeeruddin, M. K.; Grätzel, M. Nanocrystalline rutile electron extraction layer enables low-temperature solution processed perovskite photovoltaics with 13.7% efficiency. *Nano Lett.* **2014**, *14* (5), 2591– 2596, DOI: 10.1021/nl500399m

44. Gorgoi, M.; Svensson, S.; Schäfers, F.; Öhrwall, G.; Mertin, M.; Bressler, P.; Karis, O.; Siegbahn, H.; Sandell, A.; Rensmo, H.The high kinetic energy photoelectron spectroscopy facility at BESSY progress and first results. *Nucl. Instrum. Methods Phys. Res., Sect. A* **2009**, *601* (1–2), 48– 53, DOI: 10.1016/j.nima.2008.12.244

45. Schaefers, F.; Mertin, M.; Gorgoi, M. KMC-1: A high resolution and high flux soft x-ray beamline at BESSY. *Rev. Sci. Instrum.* **2007**, *78* (12), 123102, DOI: 10.1063/1.2808334

46. Wojdyr, M. Fityk: a general-purpose peak fitting program. *J. Appl. Crystallogr.* **2010**, *43* (5–1), 1126– 1128, DOI: 10.1107/S0021889810030499

47. Trzhaskovskaya, M.; Nefedov, V.; Yarzhemsky, V. Photoelectron angular distribution parameters for elements Z= 1 to Z= 54 in the photoelectron energy range 100–5000 eV. *At. Data Nucl. Data Tables* **2001**, *77* (1), 97– 159, DOI: 10.1006/adnd.2000.0849

48. Trzhaskovskaya, M.; Nefedov, V.; Yarzhemsky, V. Photoelectron angular distribution parameters for elements Z= 55 to Z= 100 in the photoelectron energy range 100–5000 eV. *At. Data Nucl. Data Tables* **2002**, *82* (2), 257– 311, DOI: 10.1006/adnd.2002.0886

49. Trzhaskovskaya, M.; Nikulin, V.; Nefedov, V.; Yarzhemsky, V. Non-dipole second order parameters of the photoelectron angular distribution for elements Z= 1–100 in the photoelectron energy range 1–10 keV. *At. Data Nucl. Data Tables* **2006**, *92* (2), 245– 304, DOI: 10.1016/j.adt.2005.12.002

50. Seah, M.; Smith, G. Quantitative AES and XPS: Determination of the electron spectrometer transmission function and the detector sensitivity energy dependencies for the production of true electron emission spectra in AES and XPS. *Surf. Interface Anal.* **1990**, *15* (12), 751– 766, DOI: 10.1002/sia.740151208

51. Scrocco, M. X-ray photoemission spectra of Pb (II) halides: A study of the satellites on the core and valence bands. *Phys. Rev. B: Condens. Matter Mater. Phys.* **1982**, *25* (3), 1535, DOI: 10.1103/PhysRevB.25.1535

52. Sadoughi, G.; Starr, D. E.; Handick, E.; Stranks, S. D.; Gorgoi, M.; Wilks, R. G.; Bär, M.; Snaith, H. J. Observation and mediation of the presence of metallic lead in organic–inorganic perovskite films. *ACS Appl. Mater. Interfaces* **2015**, *7* (24), 13440– 13444, DOI: 10.1021/acsami.5b02237

53. Stoumpos, C. C.; Malliakas, C. D.; Kanatzidis, M. G. Semiconducting tin and lead iodide perovskites with organic cations: phase transitions, high mobilities, and near-infrared photoluminescent properties. *Inorg. Chem.* **2013**, *52* (15), 9019– 9038, DOI: 10.1021/ic401215x

54. Perdew, J. P.; Burke, K.; Ernzerhof, M. Generalized Gradient Approximation Made Simple. *Phys. Rev. Lett.* **1996**, *77* (18), 3865, DOI: 10.1103/PhysRevLett.77.3865

55. Van de Walle, C. G.; Neugebauer, J. First-principles calculations for defects and impurities: Applications to III-nitrides. *J. Appl. Phys.* **2004**, *95* (8), 3851– 3879, DOI: 10.1063/1.1682673

56. Meggiolaro, D.; De Angelis, F. First-Principles Modeling of Defects in Lead Halide Perovskites: Best Practices and Open Issues. *ACS Energy Letters* **2018**, *3* (9), 2206– 2222, DOI: 10.1021/acsenergylett.8b01212

57. Heyd, J.; Scuseria, G. E.; Ernzerhof, M. Hybrid functionals based on a screened Coulomb potential. *J. Chem. Phys.* **2003**, *118* (18), 8207– 8215, DOI: 10.1063/1.1564060

58. Grimme, S.; Antony, J.; Ehrlich, S.; Krieg, H. A consistent and accurate ab initio parametrization of density functional dispersion correction (DFT-D) for the 94 elements H-Pu. *J. Chem. Phys.* **2010**, *132* (15), 154104, DOI: 10.1063/1.3382344

59. Thompson, P.; Cox, D.; Hastings, J. Rietveld refinement of Debye–Scherrer synchrotron X-ray data from Al2O3. *J. Appl. Crystallogr.* **1987**, *20* (2), 79– 83, DOI: 10.1107/S0021889887087090

60. Stolterfoht, M.; Wolff, C. M.; Márquez, J. A.; Zhang, S.; Hages, C. J.; Rothhardt, D.; Albrecht, S.; Burn, P. L.; Meredith, P.; Unold, T.; Neher, D. Visualization and suppression of interfacial recombination for high-efficiency large-area pin perovskite solar cells. *Nature Energy* **2018**, *3* (10), 847, DOI: 10.1038/s41560-018-0219-8

61. Delamarre, A.; Lombez, L.; Guillemoles, J.-F. Contactless mapping of saturation currents of solar cells by photoluminescence. *Appl. Phys. Lett.* **2012**, *100* (13), 131108, DOI: 10.1063/1.3697704

62. Unold, T.; Gütay, L. Photoluminescence analysis of thin-film solar cells. In *Advanced Characterization Techniques for Thin Film Solar Cells*; Abou-Ras, D., Kirchartz, T., Rau, U., Eds.; Wiley-VCH Verlag GmbH & Co. KGaA., 2016; Vol. 1, pp 275– 297.